Materials Advances

ROYAL SOCIETY OF CHEMISTRY

PAPER

View Article Online
View Journal | View Issue

Cite this: *Mater. Adv.*, 2024, 5, 4409

A heterostructure nanofiber film with an enhanced internal electrical field and surface plasmon resonance for efficient microbial removal†

Wanting Li,[a] Jing Yang,[b] Xin Gao,[c] Yiqian Fu,[a] Huiyu He,[b] Pu Wang,[bde] Yudong Hou,[c] Mankang Zhu[c] and Xiu-Hong Wang*[ade]

Received 10th January 2024,
Accepted 31st March 2024

DOI: 10.1039/d4ma00026a

rsc.li/materials-advances

Severe water pollution has posed a great threat to human health and aquatic organisms, leading to serious damage to aquatic ecosystems. Reactive oxygen species is essential in the degradation of water pollutants *via* a redox reaction. Here we report boosted and controllable generation of reactive oxygen species and subsequent removal of organics through ultrasonic and light-activated photo-piezocatalysis enabled by a nanofiber film. A Ag@$BaTiO_3$ nano hybrid seeded polyvinylidene fluoride (PVDF) composite fiber film with enhanced β phase content was fabricated using electrospinning. The piezoelectric device made of the Ag@$BaTiO_3$/PVDF fiber film displayed enhanced piezoelectric performance, with an open circuit voltage of approximately 6.3 V and a short circuit current of 0.497 μA under 3.39 N pressure. The rate of reactive oxygen species generated *via* continued ultrasonic irradiation of the heterostructured fiber film is significantly faster than that of the pure PVDF film. The film allows efficient degradation of water pollutants (degradation rate 81%) and removal of microbial species (99% clearance of *E. coli) via* a concerted route of photo-piezocatalysis. In summary, the use of a heterostructured PVDF nanofiber film is an effective approach to induce an integral electrical field and to piezocatalytically generate aqueous ROS, which is desirable in environmental pollution control.

1. Introduction

The increased attention paid to global environmental protection together with the world water shortage has encouraged research into cleansing and conservation of water resources. Severe water pollution has posed a great threat to human health and aquatic organisms, leading to serious damage to aquatic ecosystems. The emissions of organic and bacterial pollutants in water are increasing at an alarming rate, and post-treatment is urgently needed for dealing with water pollution.[1] In the past, photocatalysis has been widely used as a safe environmental purification strategy. However, the high recombination rate of photon induced carriers and low catalysis efficiency in the visible range hinder the further development of this technology.[2–4]

Recently, piezoelectric catalysis, which makes up for the deficiency of photocatalysis to some extent, has attracted unprecedented research interest in the areas of environmental remediation and energy conversion. In piezocatalysis, the polarization induced by strain or pressure can generate charges and free carriers that can react with H_2O and O_2 molecules in the environment generating reactive oxygen species (ROS), which are highly active substances for catalysis of reduction–oxidation (red–ox) reactions.[5–7] Common piezoelectric ceramic materials, such as potassium sodium niobate (KNN),[8] barium titanate ($BaTiO_3$/BTO),[9] lead zirconate titanate (PZT),[10] calcium barium zirconate titanate (BCZT)[11] and so on, exhibit voltage at both sides when subjected to pressure. The voltage promotes the separation of electrons and holes and effectively inhibits their recombination.[4,12] Various attempts, for instance, introduction of heterojunction structures[13] and surface modification of piezoelectric ceramics by Au, Ag, Pt and other noble metals,[14] have been explored to enhance the separation of

---

[a] *Laboratory for Biomedical Photonics, School of Physics and Optoelectronic Engineering, Beijing University of Technology, 100 Pingleyuan, Chaoyang District, Beijing 100124, China. E-mail: wxh2012@bjut.edu.cn; Tel: +86-18612921803*

[b] *Laboratory for Advanced Laser Technology and Applications, School of Physics and Optoelectronic Engineering, Beijing University of Technology, Beijing 100124, China*

[c] *Key Laboratory of Advanced Functional Materials, Ministry of Education, College of Materials Science and Engineering, Beijing University of Technology, Beijing 100124, China*

[d] *Key Laboratory of Trans-scale Laser Manufacturing Technology, Ministry of Education, Beijing 100124, China*

[e] *Beijing Engineering Research Center of Laser Technology, Beijing 100124, China*

† Electronic supplementary information (ESI) available. See DOI: **https://doi.org/10.1039/d4ma00026a**

electrons and holes, thereby improving the piezoelectric catalytic performance.

One limitation of the common piezoelectric ceramic materials lies in the difficulty in catalyst recycling and thus low reusability,[15,16] very much due to their presence predominantly in the particulate phase. In this regard, some organic polymers with a high piezoelectric coefficient and flexibility, including polyvinylidene fluoride (PVDF),[17] polytetrafluoroethylene (PTFE),[18] polylactic acid (PLA)[19] and so forth, can effectively overcome the shortcomings of piezoelectric ceramic catalysts.[20] PVDF is a semicrystalline polymer with five crystal forms: α-phase (TGTG′), β-phase (TTTT), γ-phase (TTTGTTTG′) and δ (TGTG′) and ε,[21,22] of which the β phase exhibits the highest piezoelectric activity.[23] However, the β-phase content in PVDF is usually very low. Additional processing is required to transform the α phase and other phases into the β phase, such as mechanical stretching,[24] anodization, high-temperature quenching,[25] and corona polarization. Recent research on PVDF nanofiber films prepared by electrospinning has shown that electrospinning can effectively promote β-phase PVDF generation,[26] greatly simplifying the complicated steps of piezoelectrically active PVDF film preparation.

In this context, the overall objective of this research was to enhance the piezoelectric properties of the PVDF film *via* doping Ag@BTO heterostructured nanoparticles to achieve efficient catalytic performance. Herein, Ag@BTO nanofillers were embedded into an electrospun PVDF nanofiber film. The advantages of the as-prepared heterostructured fiber film include enhanced piezoelectric performance, and thus boosted photo-piezocatalytic activity for degradation of water pollutants. In addition, compared with the piezoelectric ceramic materials, thin film catalytic materials have better flexibility and thus are easier to recycle and reuse. A Ag@BTO heterostructure seeded PVDF nanofiber film was fabricated using electrospinning and its piezoelectrical properties, the ability to generate reactive oxygen species, and as a water cleanser, the ability to remove organic pollutants, were investigated. We found that adding inorganic piezoelectric materials to PVDF can not only additionally enhance the piezoelectric properties of PVDF, but they also serve as a nucleating agent for promoting β-phase formation of PVDF. The enhanced piezoelectric properties of the Ag@BTO/PVDF nanofiber film and boosted production of reactive oxygen species enabled highly efficient removal of organics in water *via* joint photo- and piezo-catalysis.

2. Experimental section

2.1 Materials

Barium acetate, acetic acid, titanium butoxide and ethanol were purchased from Aladdin. Silver nitrate, *N*,*N*-dimethylformamide (DMF), methylene blue (MB) and rhodamine B (RhB) were purchased from Macklin. Polyvinylidene fluoride (PVDF) was obtained from Sigma-Aldrich, and 1,3-diphenylisobenzofuran (DPBF) was obtained from Bide Pharmaceutical. Acetone was purchased from Beijing Tongguang Fine Chemical Company. *Escherichia coli* was purchased from BeNa Culture Collection.

2.2 Preparation of barium titanate (BTO) nanoparticles

Tetragonal barium titanate (BTO) nanoparticles were prepared by the sol–gel method, which has emerged as one of the most effective methods to prepare high-quality nanomaterials due to the advantages of simple, easy to control, low reaction and heat treatment temperature, fine product size, narrow distribution, and low impurity content. Briefly, barium acetate was dissolved in acetic acid with a molar ratio of 1 : 10, and then a certain amount of deionized water was added to the mixture. Barium acetate was stirred continuously at room temperature until it was completely dissolved. Titanium butoxide and ethanol were mixed in a molar ratio of 1 : 5. Then barium acetate solution was added dropwise to the above solution. The sol gradually thickened and became a gel through continuously stirring. The wet gel was put into a vacuum oven to dry at 180 °C overnight. The dried gel was ground in a mortar. Subsequently, it was placed in a tube furnace and calcined at 1000 °C for 10 hours.

2.3 Preparation Ag@BTO nanoparticles by a photoreduction method

Ag@BTO nanoparticles were prepared by a photoreduction method. A certain amount of barium titanate nanoparticles was weighed into a beaker, and 0.01 M silver nitrate solution was added to the beaker and stirred evenly. The suspension was irradiated with an ultraviolet lamp for 5 min to induce a photoreduction reaction. Then the suspension was poured into a centrifuge tube for centrifugation at 5000 rpm and the Ag@BTO nanoparticle precipitate was obtained. Then Ag@BTO nanoparticles were washed three times with deionized water and dried in a vacuum oven. Finally 5 wt% Ag@BTO nanoparticles were obtained.

2.4 Preparation of BTO/PVDF and the Ag@BTO/PVDF composite fiber

The nanofiber film was prepared using an electrospinning technique, and the process is illustrated in Fig. S1 (ESI†). A mixture of DMF and acetone with a volume ratio of 3 : 2 was prepared, and 20 wt% PVDF powder was put into the solvent and stirred at 60 °C until completely dissolved. Then 10 wt% BTO nanoparticles and Ag@BTO nanoparticles were separately added into the PVDF solution and ultrasonication was performed for 1 h to obtain a stable solution. The spinning solution was filled in a 5 mL syringe with an injection rate of 0.13 mm min^{-1}, the distance between the syringe and the collector was 15 cm and the applied voltage was 15 kV. The drum rotation speed was fixed to be 1000 rpm.

2.5 Fabrication of a flexible piezoelectric nanogenerator (PENG)

The electrospun film on the aluminium foil was cut to a rectangular sample size of 4 cm × 1.5 cm. The PET-ITO electrode was used as the electrode and support structure. The PVDF film was centred between two electrode layers, with the electrode size slightly smaller than the film size to prevent short circuits from occurring. Copper foil strips of a size of 0.5 cm × 5 cm were attached to the electrodes on both sides as wires. Finally, PI tape was used for encapsulation. The whole device was a "sandwich" structure.

2.6 Techniques for characterization

An X-ray diffractometer (XRD, BRUKER D8 ADVANCE) was used to analyse the sample conformation within the range of 2θ = 10°–90°. Fourier transform infrared (FTIR) analysis was performed on the sample using a Fourier transform infrared spectrometer (BRUKER INVENIO-S) to determine the phase content in barium titanate nanoparticles and PVDF nanofibers. The absorption spectrum of barium titanate nanoparticles and silver modified barium titanate nanoparticles were determined by UV-visible spectroscopy (UV-Vis, Hitachi UH-4150). The morphology and size of barium titanate nanoparticles and PVDF nanofibers were analysed by field emission scanning electron microscopy (SEM, Hitachi SU8020). The elemental composition of the sample was determined using an energy dispersive spectrometer (EDS) attached to the scanning electron microscope. The microstructure of the sample was characterized using high-resolution transmission electron microscopy (HRTEM) (JEOL JEM-2100). The elemental composition of the sample was determined by X-ray photoelectron spectroscopy (XPS, Thermo Fisher ESCALAB 250Xi) and the chemical state of the sample was determined. The water contact angle of the thin film was measured using a contact angle meter (CA, Data physics TP50). A fixed pressure was applied to the PENG device using a press-mode testing system. And during the testing process, there was no relative contact or separation between the press-mode testing system and the PENG device, effectively avoiding the impact of triboelectricity on the experimental results. A digital oscilloscope (Tektronix MDO3024) was used to measure the output voltage and current of piezoelectric devices. The piezoelectric response of the PVDF fiber and the Ag@BTO/PVDF fiber was analyzed by piezoelectric force microscopy (PFM, Bruker Dimension Icon).

2.7 Measurement of photo-piezocatalytic activity

The photo-piezocatalytic properties of the prepared films were tested by various photo-piezocatalytic experiments. Photo-piezocatalytic experiments were conducted on two dyes, respectively methylene blue (MB, 5 mg L^{-1}) and rhodamine B (RhB, 5 mg L^{-1}). The volume of the dye used for photo-piezocatalytic experiments was 10 mL. The film was cut to a size of 2 cm × 2 cm, and the film was immersed in dye solution and soaked in the dark for 2 h to achieve adsorption and desorption balance. Three groups of dye solutions with different treatment methods (light, ultrasonic, and ultrasonic light) were set up respectively. An ultrasonic cleaner (40 kHz, 120 W) was used for ultrasonic treatment. In order to avoid the temperature upsurge of water due to ultrasonic heat production during the ultrasonic process, the water was replaced in time after the ultrasonication

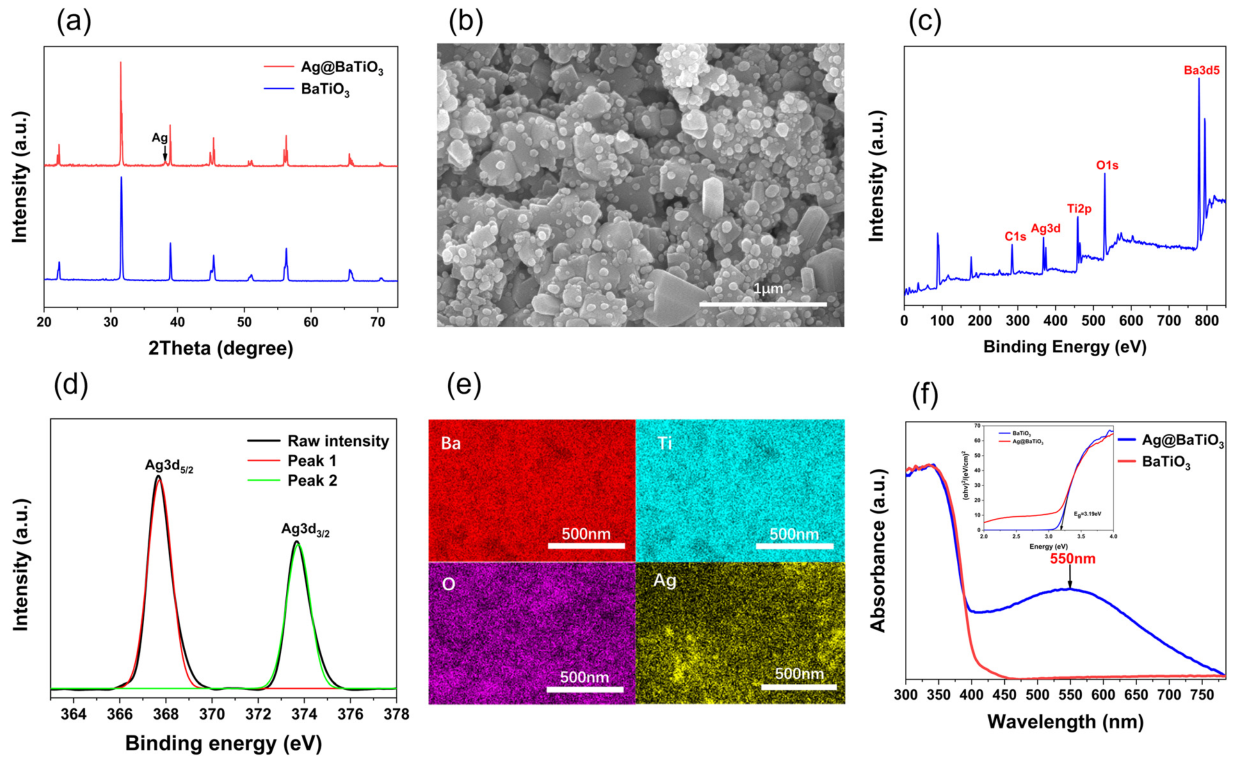

Fig. 1 Characterization of Ag@BTO. (a) XRD comparison of BTO (blue line) and Ag@BTO (red line) (b) SEM image of Ag@BTO, scale bar 1 μm. (c) XPS spectrum of Ag@BTO (d) XPS Ag3d core-level spectra of Ag@BTO (e) EDS element mapping of Ag@BTO (f) UV-Vis DRS spectra of BTO (red line) and Ag@BTO (blue line). The illustration shows band gap of BTO (blue line) and Ag@BTO (red line).

was completed. The absorbance of dye solution was measured using a microplate reader (Bio Tek Epoch), and the change of dye solution concentration in the photo-piezocatalytic process was detected.

2.8 Antibacterial experiment

Escherichia coli was used as the antibacterial experimental object. An *E. coli* single colony was placed in a conical bottle containing Luria–Bertani (L–B) broth medium and grown overnight at 100 rpm in the 37 °C constant temperature rocker rotator. The bacterial suspension diluted by phosphate-buffer saline (PBS) was transferred to a centrifuge tube for storage and a 2 cm × 2 cm film was dipped into it. Then suspensions containing the films were treated by ultrasonication and light. The control group was set as a bacterial suspension without a thin film and subjected to the same ultrasonic and light treatment. At regular intervals, 150 μL bacterial suspensions were suctioned from each of the two sets of centrifuge tubes. It was evenly dispersed on an agar plate containing L–B broth and kept overnight in an incubator at 37 °C. To calculate the survival rate of bacteria, the following formula (1) was used:[27]

$$\log\ \text{reduction} = \log_{10}\left(\frac{N_0}{N}\right) = \log_{10} N_0 - \log_{10} N \qquad (1)$$

where "N_0" is the CFU mL^{-1} count of the *E. coli* suspension at $t = 0$ min and "N" is the CFU mL^{-1} of the *E. coli* suspension at time "t" during the catalytic experiment.

3. Results and discussion

3.1 Preparation of Ag@BaTiO$_3$ (Ag@BTO) nano hybrids

First of all, BaTiO$_3$ (BTO) nanoparticles were fabricated using a sol–gel method with a calcination temperature of 1000. The particle diameter was in the range of 200–300 nm (Fig. S2a, ESI†). Most of the particles had cubic morphology. The XRD pattern of the as-prepared BTO powder shows the 2θ diffraction peak splits into two peaks at 45° (0 0 2) and 45.4° (2 0 0), indicating that the prepared barium titanate is in the tetragonal phase (JCPDS no: 05-0626) (Fig. 1(a), blue line), which is essential for its piezoelectrical properties. Below 1000 °C, the particle size decreased (Fig. S2b, ESI†) and the tetragonal phase was not observed (Fig. S2c, ESI†). The Raman spectrum of BTO nanoparticles (Fig. S3a, ESI†) displays peaks at ~188 cm^{-1} [A1(TO), E(TO), E(LO), A1(LO)], ~257 cm^{-1} [A1(TO)], ~309 cm^{-1} [B1, E(TO + LO)], ~520 cm^{-1} [A1(TO), E(TO)], and ~717 cm^{-1} [A1(LO), E(LO)], further confirming the tetragonal crystal phase.[28] The FTIR spectrum (Fig. S3b, ESI†) shows the presence of Ti–O vibration mode at 540 cm^{-1}. The mode of 1440 cm^{-1} represents the characteristic peak of barium titanate powder. The modes of 1640 cm^{-1} and 3450 cm^{-1} are assigned to the characteristic peak of OH$^-$, indicating that BTO powder contains a certain amount of water.[29]

Subsequently, Ag@BTO was prepared by using the photo-reduction method. It can be seen from Fig. 1(b) that there are

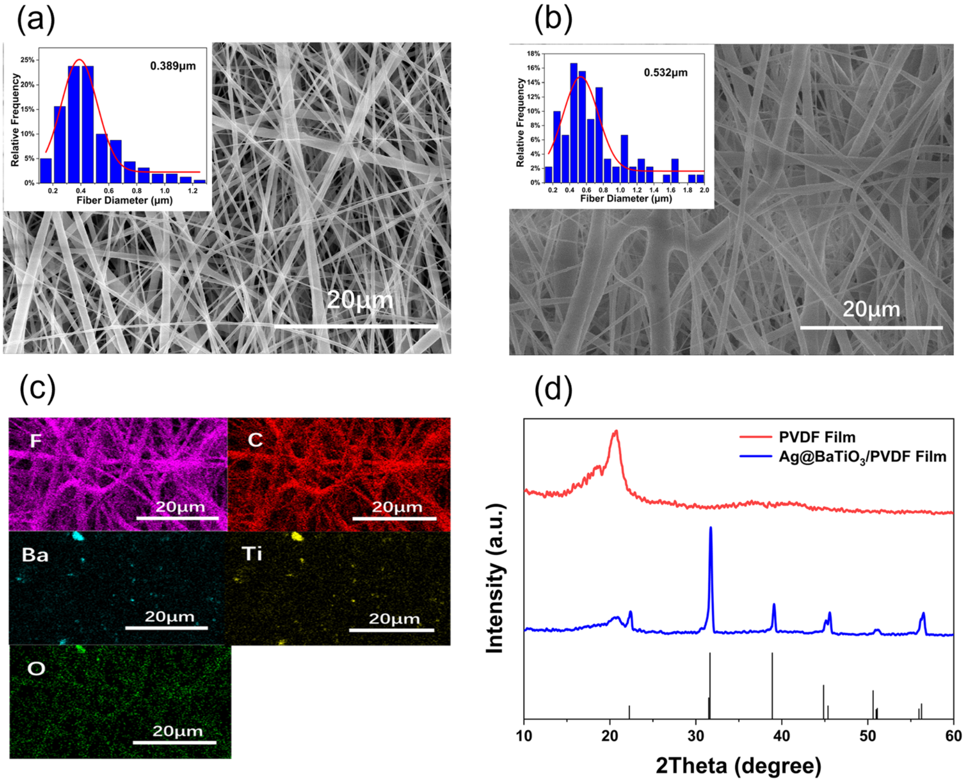

Fig. 2 Characterization of Ag@BTO/PVDF heterostructure film. (a) SEM image of the PVDF electrospun fiber film. The inset shows statistical diameter distribution of the PVDF fiber. The average diameter is 389 nm. (b) SEM image of the Ag@BTO/PVDF electrospun fiber film. The inset shows statistical diameter distribution of Ag@BTO/PVDF. The average diameter is 532 nm. (c) EDS element mapping of the Ag@BTO/PVDF fiber film (d) XRD spectra of PVDF (red line) and Ag@BTO/PVDF film (blue line).

substantial silver nanoparticles (∼10 nm) attached to the surface of BTO particles through SEM analysis (TEM further confirmed the result as shown in Fig. S4, ESI†), which is strikingly distinct from the morphology of BTO (Fig. S2a, ESI†). Some agglomerations occurred in the process of calcination. The XRD pattern (Fig. 1(a), red line) shows a weak peak at $2\theta = 38^\circ$, indicating the presence of Ag atoms. Silver nanoparticle deposition on the surface of BTO particles did not change the morphology of BTO. The presence of Ag atoms was further confirmed by XPS analysis (Fig. 1(c) and (d)).[30] The element distribution of Ag@BTO was found to be uniform through element mapping *via* energy dispersive spectroscopic (EDS) analysis (Fig. 1(e)).

The UV-visible diffuse reflectance spectra (DRS) of BTO and Ag@BTO nanoparticles are shown in Fig. 1(f). The single-phase BTO has a steep absorption edge near ∼342 nm. According to the Tauc plot, the band gap of BTO is 3.19 eV (Fig. 1(f) inset). While the steep absorption edge of Ag@BTO does not change significantly after Ag photo-deposition, and the large bandwidth absorption appears near ∼550 nm. This can be explained by the local surface plasmon resonance (LSPR) effects by Ag.[31,32] The bandgap of BTO limits its absorption of light only to the ultraviolet region of the solar spectrum, but silver nanoparticles exhibit resonance behaviour when interacting with ultraviolet and visible photons, and as a result, it leads to the light absorption of Ag@BTO light extending from the ultraviolet region around 342 nm to the visible region around 550 nm.[31] The larger bandwidth of Ag@BTO enables more efficient absorption of light energy in the visible light region compared with BTO, which is of great help to improve the efficiency of photocatalysis.

3.2 Fabrication of the Ag@BTO/PVDF film

The Ag@BTO/PVDF film was fabricated using electrospinning *via* doping 10 wt% Ag@BTO nanoparticles in 20 wt% PVDF solution. The film thickness was around 200 μm determined using a step profiler. The morphology of the PVDF film and Ag@BTO/PVDF film were observed using SEM (Fig. 2(a) and (b)). The average diameter of Ag@BTO/PVDF film was about 532 nm (Fig. 2(b) inset), larger than that of the PVDF fiber, which was about 389 nm (Fig. 2(a) inset). Among the investigated doping concentrations of Ag@BTO, the fiber diameter increased with the increase of doping concentration (Fig. S5a–d and Table S1, ESI†). We also found that, as the drum rotating speed increases, the fiber diameter decreases (Fig. S5e, ESI†). On the one hand, addition of Ag@BTO decreased the solution conductivity, and thus decreased charge density and weakened stretching of the electrospinning jet. On the other hand, it is likely that addition of Ag@BTO particles increased the viscosity of the PVDF solution, thus improving the ability of the jet to resist the stretching of the electric field. As a result, the diameter of the fiber increased.[33] We used 10 wt% Ag@BTO doping for all the following experiments.

The elemental distributions of Ba, Ti and O by EDS analysis showed good consistency as shown in Fig. 2(c). It is notable that Ag element was not displayed by EDS due to its low content; however, the XRD results of Ag@BTO/PVDF films indicated the successful doping of Ag@BTO particles (Fig. 2(d)).

The XRD spectra of PVDF powder and electrospun PVDF nanofiber films are shown in Fig. 3(a). The characteristic peaks at 18.3°, 19.9° and 26.6° representing the α phase of PVDF were significantly weakened in the electrospun PVDF fiber compared with PVDF powder; meanwhile, the crystallization peak of the β phase at 20.6° was significantly intensified. Clearly, the electrospinning process generated a higher-content β phase due to the spin–stretch operation. The results indicated that electrospinning technique was beneficial to increase the content of the β phase in PVDF.[34] This was further confirmed by Raman spectral analysis. Fig. 3(b) shows the characteristic peaks of the α phase at 796 cm^{-1}, 876 cm^{-1} and the β phase at 839 cm^{-1} of PVDF powder; obviously, the α phase was dominant. In clear contrast, the peak intensity at 839 cm^{-1} of the PVDF fiber (Fig. 3(c)) was greatly enhanced while the peak intensities at 796 cm^{-1} and 876 cm^{-1} were decreased, indicating that the electrospinning process can effectively induce phase transformation from α to β.[35]

The exact β phase content of the as-prepared films was analysed using FTIR. According to Lambert Beer's law,[36] formula (2) was used to calculate the β phase content:

$$F(\beta) = \frac{A_\beta}{\left(\frac{K_\beta}{K_\alpha}\right)A_\alpha + A_\beta} \tag{2}$$

where $F(\beta)$ represents β phase content, A_α and A_β are the absorbance of the α phase at 760 cm^{-1} and β phase at 840 cm^{-1}, respectively. K_α and K_β are the absorption coefficients of α and β phase, the specific values being 6.1×10^4 and 7.7×10^4 $\text{cm}^2\ \text{mol}^{-1}$ respectively. The β phase content of various PVDF formats was calculated using the formula (Fig. 3(d)). We can see that β phase content was in the order of Ag@BTO/PVDF film > BTO/PVDF film > PVDF film > PVDF powder. The 10 wt% Ag@BTO doped PVDF fiber film had the maximum β phase content of 83%, which is 1.5 times higher than that of PVDF powder.

The increased β phase content of Ag@BTO/PVDF nanofiber film can be explained from two aspects. Firstly, BTO nanoparticles act as nucleating agents for β-phase PVDF crystallization, and the interaction between BTO nanoparticles and PVDF chains promotes β phase formation. Strong hydrogen bonds of O–H···F–C were formed between hydrogen atoms in the hydroxyl group on BTO surface and fluorine atoms in the PVDF chain (Fig. 4).[37–39] The electrostatic attraction and repulsion between BTO nanoparticles and $-\text{CH}_2-\text{CF}_2$ dipoles of PVDF promoted PVDF chains to align along the fiber axis easily. This led to $-\text{CH}_2-\text{CF}_2$ dipoles formation and resulted in an all-*trans* (TTTT) planar sawtooth conformation orientation, which was the spatial configuration of the β phase.[40] In addition to the interfacial interaction between BTO nanoparticles and PVDF chains, the arrangement of $-\text{CH}_2-\text{CF}_2$ dipoles also depended on the dipole interaction between polar DMF solvents and PVDF chains.[41] The interface interaction between BTO and PVDF, as well as the interaction between

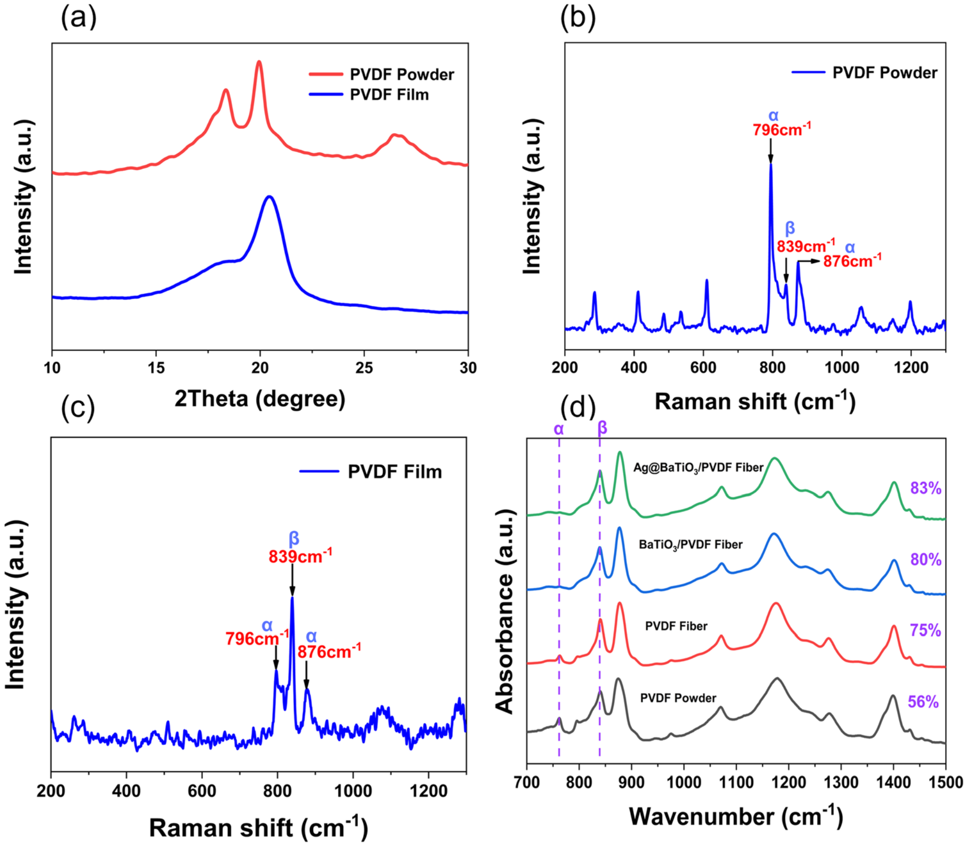

Fig. 3 Electrospinning increased β phase content (a) XRD comparison of PVDF powder and PVDF film (b) and (c) Raman spectra of PVDF powder and PVDF film (d) FTIR analysis of PVDF fiber film with different doping.

DMF and PVDF, affects the motion and arrangement of $-CH_2-CF_2$ dipoles, promoting its β-phase formation. Secondly, with the help of electrospinning, silver on the surface of BTO particles can lead to the generation of a local electric field followed by induction of charges. The induced charge on the surface of silver nanoparticles can induce PVDF chains to crystallize on the surface of silver nanoparticles β mutually, resulting in a stronger coulomb force. The coulomb force attracts PVDF chains to crystallize into the β phase on the surface of Ag@BTO nanoparticles.[37]

3.3 Enhanced electrical performance of the Ag@BTO/PVDF piezoelectric film

The electrical signal output of the fabricated nanofiber films was tested under the same experimental conditions. The voltage and current were recorded following force application at a fixed frequency (50 Hz) to the piezoelectric device using a laboratory customized press-mode system (Fig. 5(a)–(c)). The open circuit voltages of the Ag@BTO/PVDF film, BTO/PVDF film and PVDF films were about 6.2 V, 5.4 V and 3 V (Fig. 5(d)), respectively. It can be seen that the generated voltage was dependent on the β phase content of the PVDF film. Doping of BTO nanoparticles effectively improved the piezoelectric performance of the PVDF matrix. BTO nanoparticles as stress concentration points in composite fibers enhanced the internal electric field strength of the fibers. Therefore, compared to the PVDF film, the output voltage of the BTO/PVDF film was increased by 2.4 V. The silver atoms on the Ag@BTO surface of the Ag@BTO/PVDF film, not only can increase the β phase content of PVDF film as discussed above, but also can effectively capture electrons and act as a "fast channel" for electron transfer, and therefore can further increase the output voltage by 0.8 V compared to the BTO/PVDF film. A total of 3.2 V voltage increment of the Ag@BTO/PVDF film was achieved compared with the PVDF film. PFM was also used to conduct piezoelectric performance tests on the PVDF fiber film and Ag@BTO/PVDF fiber film. The testing results are shown in Fig. S6 (ESI†).

Different Ag@BTO loading may affect the viscosity of the electrospinning solution and the conductivity of the film. Therefore, the output voltages of Ag@BTO/PVDF composite fiber film with different Ag@BTO loadings (5%, 10%, 15%) were investigated. We found that 10% Ag@BTO doped PVDF fiber film showed the optimum output voltage (Fig. S7, ESI†), so the following experiments were all performed with the PVDF film of 10%Ag@BTO loading if not specified.

The force-dependent piezoelectric performance of Ag@BTO/PVDF piezoelectric device was investigated. First of all, a 0.489 N preloading force was applied to the film, and then the amplitude of the press-mode system was constantly changed, and the pressure was converted to the magnitude of the pressure applied according to the number of the force sensor on the oscilloscope. As the pressure increased, the open circuit

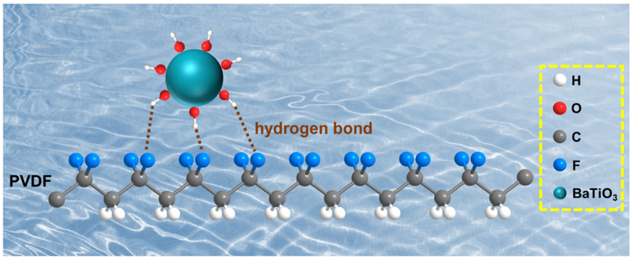

Fig. 4 Schematic diagram illustrating hydrogen bond formation between BTO and PVDF chain in the fiber film.

voltage of the Ag@BTO/PVDF piezoelectric device elevated (Fig. 5(e)). The short-circuit current shows similar variation tendency (Fig. 5(f)). When a pressure of 0.23 N was applied, the open circuit voltage and short circuit current were 0.342 V and 6.8×10^{-3} μA, respectively. As the pressure increased to 3.39 N, the voltage and current increased to 6.3 V and 0.497 μA, respectively. The sensitivity of the device was around 1.65 V N^{-1}.

To prove that the generated electrical signal was a piezoelectric signal instead of a triboelectric signal, inverse connection measurement of Ag@BTO/PVDF piezoelectric device was carried out[42] (Fig. 5(g)). It was found that the amplitude of the electrical signal also reversed, which confirmed that the electrical signal generated was a piezoelectric type.[43,44]

To confirm the result, we performed piezo force microscopic analysis of PVDF and Ag@BTO/PVDF fiber (Fig. S6, ESI†). The amplitude and phase were measured by applying voltage ranging from −10 V to +10 V while the probe was placed at a fixed position on the PVDF or Ag@BTO/PVDF single fiber. Compared to the PVDF fiber, Ag@BTO/PVDF fiber showed a well-defined butterfly curve and the maximum amplitude of Ag@BTO/PVDF was much greater than PVDF. Ag@BTO/PVDF had a significant 180° phase change hysteresis phenomenon, indicating non-zero remnant polarisation. The PFM data further confirmed that Ag@BTO reinforced PVDF fiber exhibited better piezoelectric performance than pure PVDF fiber, which is consistent with the PENG results.

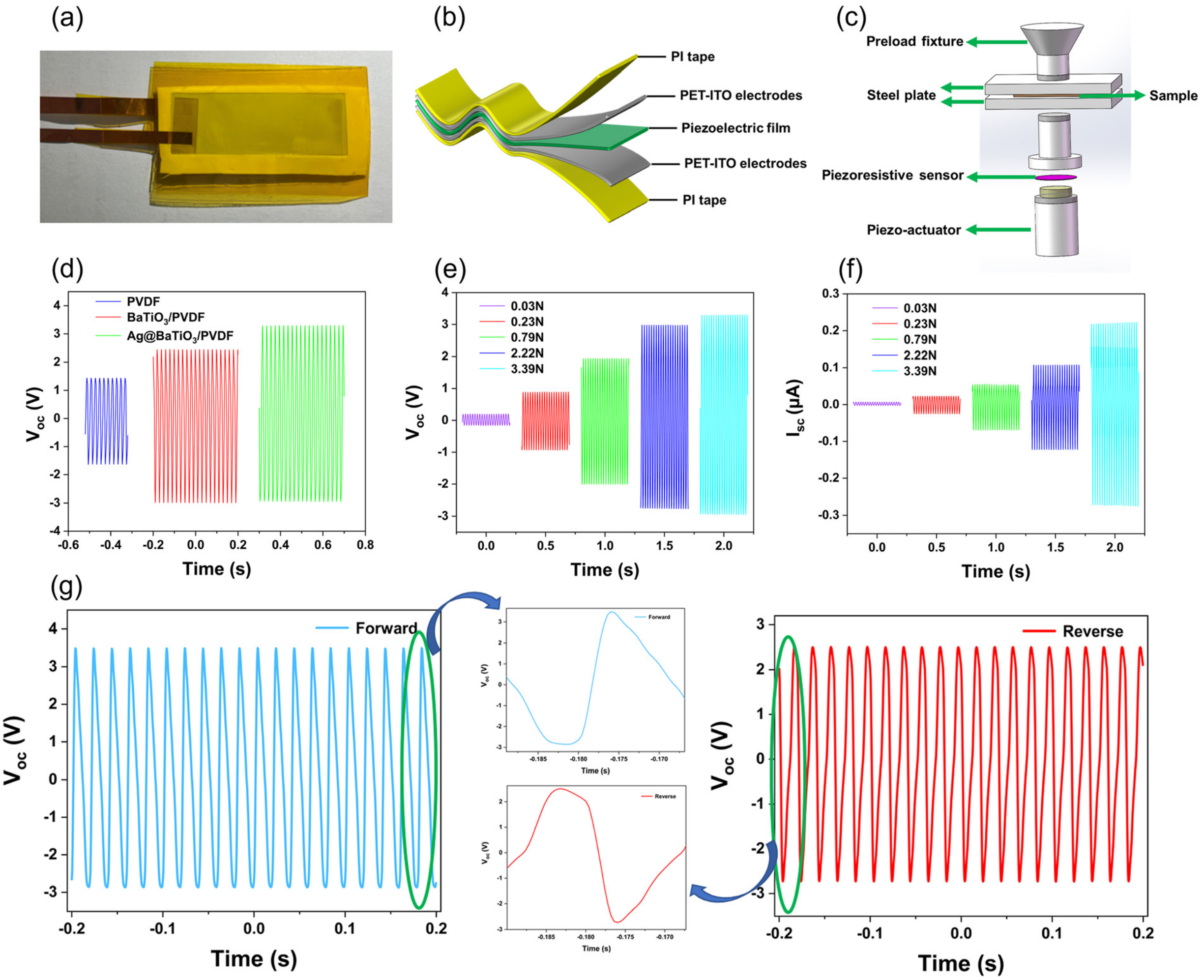

Fig. 5 Electrical properties of the piezoelectrical device. (a) Picture and (b) schematic diagram of the house-made piezoelectric device (c) schematic diagram of the press-mode test system. (d) Comparison of output voltages of PVDF films with different compositions under the same pressure (3.39 N, at a fixed frequency of 50 Hz) (e) Pressure-dependent open circuit voltages of the Ag@BTO/PVDF film. (f) Pressure-dependent short circuit currents of the Ag@BTO/PVDF film. (g) Forward and reverse voltage comparison of the Ag@BTO/PVDF film.

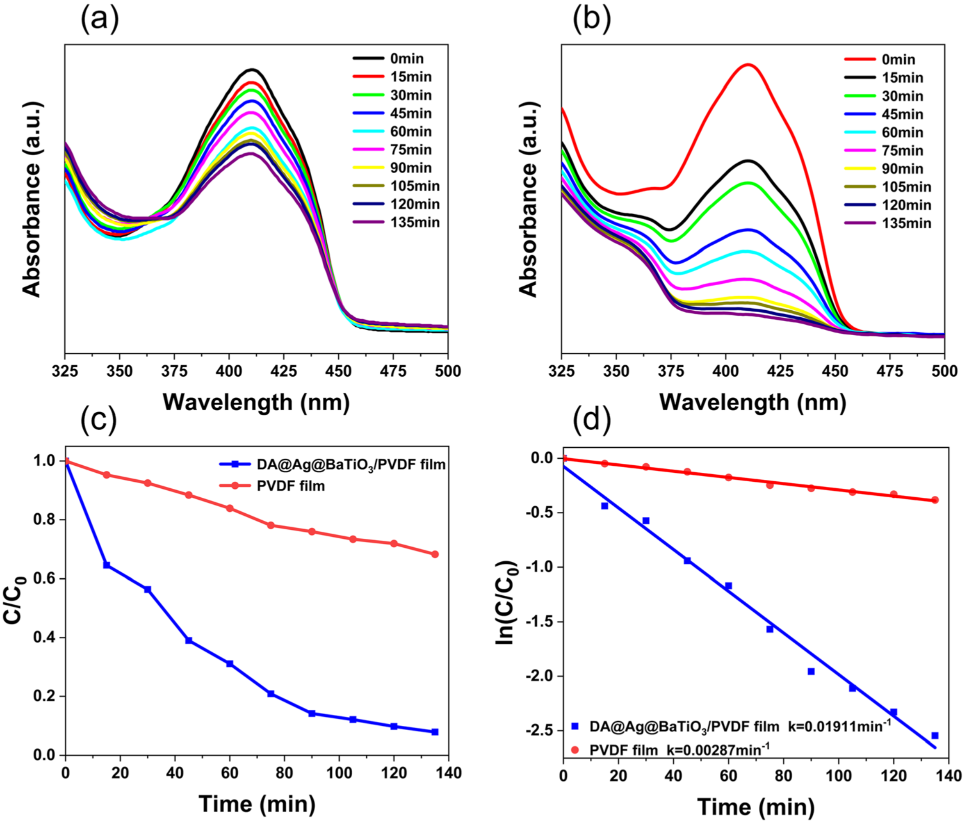

Fig. 6 Enhanced ROS generation by the Ag@BTO/PVDF film. UV-Vis spectra of DPBF following continued ultrasonic treatment with (a) Ag@BTO/PVDF film and (b) PVDF film (c) variation in DPBF concentration (C/C_0) over vibration time t with Ag@BTO/PVDF and PVDF films. (d) Rate of catalytic DPBF degradation over the vibration time t with Ag@BTO/PVDF and PVDF films.

3.4 Improved and controlled ROS generation by using the Ag@BTO/PVDF film

The piezocatalytic mechanism is largely dependent on the generation of free charge carriers when the film is exposed to ultrasonic irradiation. Ultrasonication causes the film to deform, so that the film converts mechanical energy into electrical energy. An electric field was formed on the surface of the film, instantly forming two surfaces with positive and negative polarity. Due to the attraction/repulsion effects of electrons (e^-) and holes (h^+) on the film surface, free charge carriers will move in the opposite direction of the polarization field. During the movement, free charge carriers interact with O_2 and OH^- in water to form reactive oxygen species ($^{\bullet}O_2^-$ and $^{\bullet}OH$),[45] as shown in formulas (3)–(6). Reactive oxygen species (ROS) degrade organic pollutants *via* a redox reaction.

$$\text{Ag@BaTiO}_3\text{/PVDF} + \text{ultrasound/photon} \rightarrow e^- + h^+ \quad (3)$$

$$O_2\ (\text{absorbed}) + e^- \rightarrow {}^{\bullet}O_2^- \quad (4)$$

$$OH^-\ (\text{from } H_2O) + h^+ \rightarrow {}^{\bullet}OH^- \quad (5)$$

$$\text{Dye/bacteria} + \text{ROS}({}^{\bullet}OH^-/{}^{\bullet}O_2^-) \rightarrow \text{Degradation products} \quad (6)$$

The ROS generated by ultrasonication was determined using a ROS probe: 1,3-diphenylisobenofuran (DPBF), which is a singlet oxygen ($^1O_2$) scavenger.[46] The Ag@BTO/PVDF film and PVDF film were immersed into 50 μM DPBF solution followed by ultrasonic (US) treatment in the dark. For both Ag@BTO/PVDF and PVDF film treated DPBF solutions, the absorbance values at 411 nm decreased following ultrasonic irradiation, showing time-dependent $^1O_2$ generation (Fig. 6(a) and (b)). After 135 min of US treatment, the relative residual quantity of DPBF expressed by C/C_0, where C and C_0 represent MB concentration at time t and the initial concentration, respectively, was 0.08 for Ag@BTO/PVDF film; whereas it was 0.68 for PVDF film (Fig. 6(c)). The degradation rate of DPBF for Ag@BTO/PVDF film was about 6.65 times higher than that of the PVDF film (Fig. 6(d)). Clearly, Ag@BTO/PVDF nanofiber film demonstrated greater capacity to generate ROS than the PVDF film without any doping, which is consistent with the piezoelectric performance as described above.

The generation of ROS is controllable. Withdrawal of ultrasonic irradiation resulted in the direct pause in ROS production.

3.5 Photo-piezocatalytic degradation of organic dye

Having demonstrated the enhanced ROS generation, we then evaluated the catalytic performance of the Ag@BTO/PVDF film. Since the catalytic reaction occurs in the aqueous phase, to ensure efficient catalysis, we first increased the hydrophilicity

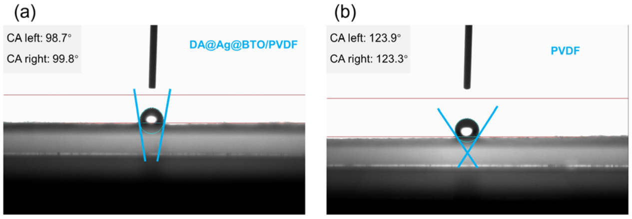

Fig. 7 Water contact angle of (a) DA@Ag@BTO/PVDF fiber film (average 99.3°) (b) PVDF film (average 123.6°).

of the film. To this end, the Ag@BTO nanoparticles were modified with dopamine (DA) before being seeded in the PVDF film. Surface functionalization of ceramic nanoparticles with organic coating could significantly improve the distribution and interface bonding between the polymer and the nano-filler, thus improving the hydrophilic performance.[47] The water contact angle of dopamine-modified Ag@BTO/PVDF fiber film (DA@Ag@BTO/PVDF) was 99°, in contrast to 129° water contact angle of the PVDF fiber film (Fig. 7(a) and (b)), indicating that the hydrophilicity of the film had been improved efficiently. The effects of dopamine modification on the piezoelectric properties of composite fiber films were investigated. Compared with the Ag@BTO/PVDF fiber film, the output voltage of the DA@Ag@BTO/PVDF fiber film was slightly increased by 0.5 V (Fig. S8, ESI†), indicating that dopamine modification can not only enhance the hydrophilicity of composite films, but also improve the piezoelectric properties slightly. The following experiments were all performed with DA@Ag@BTO/PVDF fiber film if not specified.

To evaluate the performance of the as-prepared film, catalytic degradation of organic dye methylene blue (MB, 5 mg L^{-1}) by the DA@Ag@$BaTiO_3$/PVDF nanofiber film was investigated. The film was immersed into MB solution followed by continued ultrasonication. The absorbance at 663 nm of the dye solution was measured at different time points. A time dependent change of the absorbance was observed (Fig. 8(a)). For comparison, we also investigated the photocatalysis (385 nm UV and a 532 nm green light treatment) and photo-piezocatalysis (dual light and ultrasonic treatment) behaviour of the film (Fig. 8(b) and (c)). The performance of catalytic degradation of MB was judged by the relationship between C/C_0 and time t. Three types of catalyses all demonstrated time dependent degradation of MB as shown in Fig. 8(d). Ultrasonic treatment of MB solution in dark for 135 min resulted in 72% degradation of MB; while dual-wavelength light treatment for 135 min resulted in 45.5% degradation of MB. The most efficient degradation was found for the joint ultrasonic and light treatment. The degradation ratio reached 81% after 135 min treatment (which is 62% with Ag@BTO/PVDF film without DA treatment (Fig. S9, ESI†)). Our data, on the one hand, indicate that piezocatalysis is much more effective than photocatalysis; also suggest that joint photo- and piezo-catalysis is the most promising strategy.

The degradation process follows pseudo-first-order kinetics, where the degradation rate of the dye can be calculated using

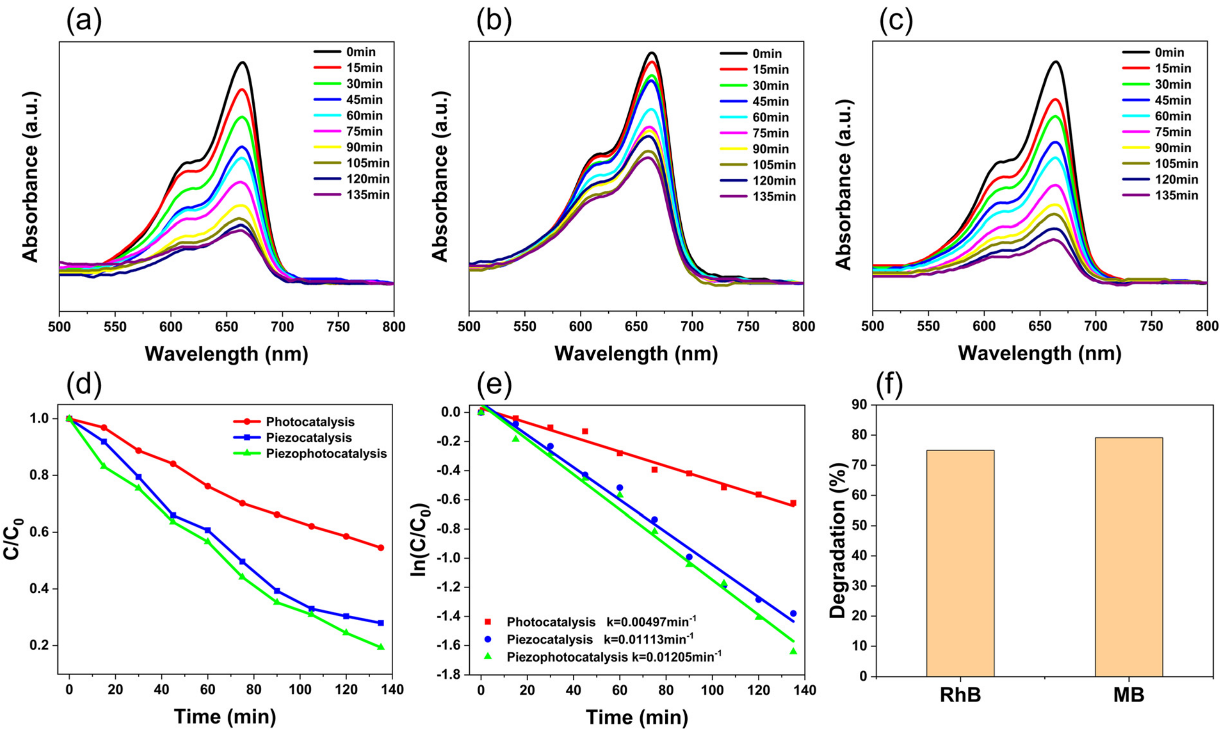

Fig. 8 Catalytic degradation of MB. UV-vis spectra of MB solution under (a) ultrasonic irradiation (piezocatalysis); (b) light irradiation (photocatalysis) and (c) dual treatment (photo-piezocatalysis) (d) time-dependent variation of MB concentration upon three types of treatment (e) catalysis rate of MB degradation upon three types of treatment (f) degradation percentages of MB and RhB through photo-piezocatalysis using the DA@Ag@BTO/PVDF composite film.

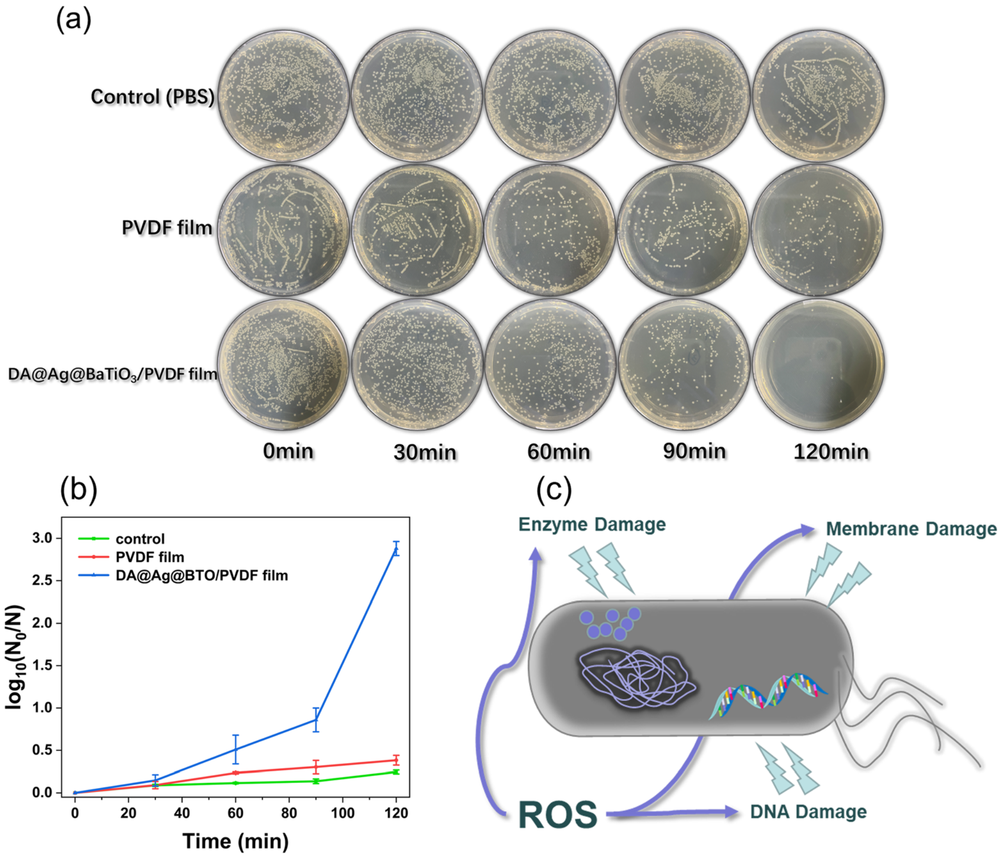

Fig. 9 Antibacterial properties of DA@Ag@BTO/PVDF film *via* photo-piezocatalysis. (a) Bacterial colonies of *E. coli* on L–B agar culture medium at various times *t* of light and ultrasonic treatment (diluted by a factor of 1.5×10^5). (b) Time dependent log reduction of CFUs mL^{-1} of *E. coli* after 120 min continued treatment, (c) schematic diagram of antibacterial mechanisms of ROS generated by photo-piezocatalysis.

formula (7).[48]

$$\ln\left(\frac{C}{C_0}\right) = -k \times t \tag{7}$$

where k is the rate constant of dye degradation, t is the treatment time. The calculated rate constants of photocatalysis, piezocatalysis and photo-piezocatalysis of the DA@Ag@BTO/PVDF nanofiber film for MB degradation were 0.00497 min^{-1}, 0.01113 min^{-1}, and 0.01205 min^{-1}, respectively. The photo-piezocatalysis rate is 2.4 times and 1.1 times higher than that of photocatalysis and piezocatalysis alone, respectively (the k values are shown in Fig. 8(e)). The piezoelectric catalysis degradation rate is 2.2 times higher than the photocatalytic degradation rate, which indicates that the piezoelectric catalysis is dominant in the synergistic catalysis process.

Photo-piezocatalysis experiments on the rhodamine B (RhB) dye also conducted using the prepared DA@Ag@BTO/PVDF films. The degradation rate of photo-piezocatalysis was 75% at 135 min (Fig. S10, ESI† and Fig. 8(f)). This indicates that the photo-piezocatalysis performance of the composite film is universal for a wide range of organic molecules. The DA@Ag@BTO/PVDF film provides a flexible platform for efficient removal of organic pollutants *via* either single-mode catalysis or joint photo-piezocatalysis.

3.6 Antibacterial properties of DA@Ag@BTO/PVDF film *via* photo-piezocatalysis

The antibacterial performance against Gram-negative *Escherichia coli* (*E. coli*) was investigated using DA@Ag@BTO/PVDF film. The film was immersed in bacterial suspension diluted using phosphate-buffer saline (PBS). Fig. 9(a) demonstrated the disinfection performance of DA@Ag@BTO/PVDF film upon US and light treatment over time. It can be clearly observed that after the bacterial suspension was treated by the DA@Ag@BTO/PVDF composite film exposed to ultrasonic waves and light for 120 min, the highest reduction of *E. coli* logarithm value (CFU mL^{-1}) of 2.94 was obtained (Fig. 9(b)). More than 99% *E. coli* bacteria were removed. In contrast, following the same period of treatment, the logarithmic reduction values of *E. coli* for PVDF film and control (PBS) samples were only 0.34 and 0.23, respectively, much lower than that of the DA@Ag@BTO/PVDF film. The clearance rates of *E. coli* were 74% and 42% respectively. We also conducted antimicrobial experiments on *E. coli* using a Ag@BTO/PVDF fiber film under same experimental conditions. The sterilization rate of *E. coli* using Ag@BTO/PVDF fiber film is about 77%, lower than DA@Ag@BTO/PVDF film (Fig. S11, ESI†).

The possible mechanism that ROS kill bacteria is illustrated in Fig. 9(c). ROS first act on the cell membrane, causing metabolic disorders and inhibiting growth; going a step further, ROS penetrate and damage the cell membrane, leading to cytolysis and cell death. In addition to ROS, silver nanoparticles can also exhibit good antibacterial properties through contact or non-contact (release of silver ions) with bacteria,[49] therefore the silver nanoparticles in the Ag@BTO/PVDF film have synergistic antibacterial effects with the generated reactive oxygen species. In the process of piezoelectric catalysis, the rupture of acoustic cavitation bubble caused by ultrasonic waves also played a role in killing bacteria to some extent.[50]

4. Conclusions

In summary, herein, we fabricated a high β phase content Ag@BTO/PVDF fiber film. The open circuit voltage and short circuit current of PVDF, BTO/PVDF and Ag@BTO/PVDF films were compared. The Ag@BTO/PVDF fiber films exhibited the best electrical properties. The PENG device with an area of 6 cm^2 prepared by using a Ag@BTO/PVDF fiber film could generate a stable open circuit voltage of 6.3 V and a short circuit current of 0.45 μA at 3.39 N pressure and 50 Hz frequency. The photo-piezocatalytic degradation of MB dye and water disinfection with the Ag@BTO/PVDF fiber film with continued ultrasonic and light irradiation were investigated. The data indicate that use of a heterostructured PVDF nanofiber film is an effective approach to induce integral electrical field and to piezocatalytically generate aqueous ROS, which is desirable in environmental pollution control. In addition, the filmy format of catalytic material renders it easy to recycle and reuse, and the controllable generation of ROS ensures the flexibility of the process. The development of new hybrid catalytic material with high efficiency and sustainability will bring economic benefits.

Data availability

Data will be made available on request.

Conflicts of interest

The authors declare that they have no known competing financial interests or personal relationships that could have appeared to influence the work reported in this paper.

Acknowledgements

This work was supported by the National Natural Science Foundation of China under grant no: 92053116 & 62035002. The authors thank Beijing University of Technology Core Facilities for technical support.

References

1 S. Verma, M. Sharma and R. Vaish, *Environ. Sci.: Nano*, 2022, **9**, 3885–3899.

2 C. Y. Dong, C. Lian, S. C. Hu, Z. S. Deng, J. Q. Gong, M. D. Li, H. L. Liu, M. Y. Xing and J. L. Zhang, *Nat. Commun.*, 2018, **9**, 11.

3 M. Xiao, Z. L. Wang, M. Q. Lyu, B. Luo, S. C. Wang, G. Liu, H. M. Cheng and L. Z. Wang, *Adv. Mater.*, 2019, **31**, 23.

4 Z. Z. Ai, K. Zhang, D. Shi, B. Chang, Y. L. Shao, L. Zhang, Y. Z. Wu and X. P. Hao, *Nano Energy*, 2020, **69**, 10.

5 H. W. Huang, S. C. Tu, C. Zeng, T. R. Zhang, A. H. Reshak and Y. H. Zhang, *Angew. Chem., Int. Ed.*, 2017, **56**, 11860–11864.

6 H. L. Su, C. C. Chou, D. J. Hung, S. H. Lin, I. C. Pao, J. H. Lin, F. L. Huang, R. X. Dong and J. J. Lin, *Biomaterials*, 2009, **30**, 5979–5987.

7 Y. Li, W. Zhang, J. F. Niu and Y. S. Chen, *ACS Nano*, 2012, **6**, 5164–5173.

8 X. X. Sun, R. C. Li, Z. W. Yang, N. Zhang, C. Wu, J. H. Li, Y. L. Chen, Q. Chen, J. Zhang, H. J. Yan, X. Lv and J. G. Wu, *Appl. Catal., B*, 2022, **313**, 11.

9 Y. D. Yao, Y. M. Jia, Q. C. Zhang, S. Li, G. R. Li, X. Z. Cui and Z. Wu, *J. Alloys Compd.*, 2022, **905**, 8.

10 S. Verma, M. Sharma, A. Halder and R. Vaish, *Surf. Interfaces*, 2022, **30**, 10.

11 K. S. Chary, V. Kumar, C. D. Prasad and H. S. Panda, *J. Aust. Ceram. Soc.*, 2020, **56**, 1107–1117.

12 C. Y. Yang, P. Wang, J. N. Li, Q. Wang, P. Xu, S. J. You, Q. Z. Zheng and G. S. Zhang, *Chem. Eng. J.*, 2021, **417**, 17.

13 Y. Yang, S. H. Zhao, F. K. Bi, J. F. Chen, Y. X. Wang, L. F. Cui, J. C. Xu and X. D. Zhang, *Appl. Catal., B*, 2022, **315**, 14.

14 X. L. Zhang, B. B. Han, Y. X. Wang, Y. Liu, L. Chen and Y. J. Zhang, *Molecules*, 2019, **24**, 12.

15 B. Bagchi, N. A. Hoque, N. Janowicz, S. Das and M. K. Tiwari, *Nano Energy*, 2020, **78**, 11.

16 W. Q. Qian, K. Zhao, D. Zhang, C. R. Bowen, Y. H. Wang and Y. Yang, *ACS Appl. Mater. Interfaces*, 2019, **11**, 27862–27869.

17 B. W. Jiang, X. X. Xue, Z. X. Mu, H. Y. Zhang, F. Li, K. Liu, W. Q. Wang, Y. F. Zhang, W. H. Li, C. Yang and K. W. Zhang, *Molecules*, 2022, **27**, 12.

18 Y. F. Wang, Y. M. Xu, S. S. Dong, P. Wang, W. Chen, Z. D. Lu, D. J. Ye, B. C. Pan, D. Wu, C. D. Vecitis and G. D. Gao, *Nat. Commun.*, 2021, **12**, 8.

19 Y. L. Xu, L. Jin, X. B. He, X. Huang, M. L. Xie, C. F. Wang, C. L. Zhang, W. Q. Yang, F. B. Meng and J. Lu, *J. Mater. Chem. A*, 2019, **7**, 1810–1823.

20 G. I. Dzhardimalieva, A. K. Zharmagambetova, S. E. Kudaibergenov and I. E. Uflyand, *Kinet. Catal.*, 2020, **61**, 198–223.

21 A. Itoh, Y. Takahashi, T. Furukawa and H. Yajima, *Polym. J.*, 2014, **46**, 207–211.

22 Y. B. Bai, Y. A. Liu, H. Lv, H. P. Shi, W. Zhou, Y. Liu and D. G. Yu, *Polymers*, 2022, **14**, 38.

23 B. Mohammadi, A. A. Yousefi and S. M. Bellah, *Polym. Test.*, 2007, **26**, 42–50.

24 Y. Zhou, W. T. Liu, B. Tan, C. Zhu, Y. R. Ni, L. Fang, C. H. Lu and Z. Z. Xu, *Polymers*, 2021, **13**, 18.

25 P. Malik, V. Gupta, H. K. Mishra, A. Kumar and D. Mandal, *J. Appl. Polym. Sci.*, 2023, **140**, 8.

26 J. S. Andrew and D. R. Clarke, *Langmuir*, 2008, **24**, 670–672.

27 G. Singh, S. Kumar, M. Sharma and R. Vaish, *J. Am. Ceram. Soc.*, 2019, **102**, 5127–5137.

28 Y. Shiratori, C. Pithan, J. Dornseiffer and R. Waser, *J. Raman Spectrosc.*, 2010, **38**, 1288–1299.

29 M. A. M. Khan, S. Kumar, J. Ahmed, M. Ahamed and A. Kumar, *Mater. Chem. Phys.*, 2021, **259**, 16.

30 E. Z. Lin, J. Wu, N. Qin, B. W. Yuan and D. H. Bao, *Catal. Sci. Technol.*, 2018, **8**, 4788–4796.

31 S. Linic, P. Christopher and D. B. Ingram, *Nat. Mater.*, 2011, **10**, 911–921.

32 C. L. Wang and D. Astruc, *Chem. Soc. Rev.*, 2014, **43**, 7188–7216.

33 J. Jiang, S. J. Tu, R. F. Fu, J. J. Li, F. Hu, B. Yan, Y. C. Gu and S. Chen, *ACS Appl. Mater. Interfaces*, 2020, **12**, 33989–33998.

34 J. J. Li, S. Chen, W. T. Liu, R. F. Fu, S. J. Tu, Y. H. Zhao, L. Q. Dong, B. Yan and Y. C. Gu, *J. Phys. Chem. C*, 2019, **123**, 11378–11387.

35 G. Y. Li, H. D. Zhang, K. Guo, X. S. Ma and Y. Z. Long, *Mater. Res. Express*, 2020, **7**, 7.

36 P. Thakur, A. Kool, N. A. Hoque, B. Bagchi, F. Khatun, P. Biswas, D. Brahma, S. Roy, S. Banerjee and S. Das, *Nano Energy*, 2018, **44**, 456–467.

37 K. M. Shi, B. Sun, X. Y. Huang and P. K. Jiang, *Nano Energy*, 2018, **52**, 153–162.

38 S. F. Mendes, C. M. Costa, C. Caparros, V. Sencadas and S. Lanceros-Méndez, *J. Mater. Sci.*, 2012, **47**, 1378–1388.

39 B. S. Athira, A. George, K. V. Priya, U. S. Hareesh, E. B. Gowd, K. P. Surendran and A. Chandran, *ACS Appl. Mater. Interfaces*, 2022, 12, DOI: **10.1021/acsami.2c07911**.

40 H. Shao, J. Fang, H. X. Wang and T. Lin, *RSC Adv.*, 2015, **5**, 14345–14350.

41 M. Kim, S. Lee and Y. I. Kim, *APL Mater.*, 2020, **8**, 9.

42 J. C. Li, J. Yin, M. G. V. Wee, A. Chinnappan and S. Ramakrishna, *Adv. Fiber Mater.*, 2023, **5**, 1417–1430.

43 C. J. Chen, S. L. Zhao, C. F. Pan, Y. L. Zi, F. C. Wang, C. Yang and Z. L. Wang, *Nat. Commun.*, 2022, **13**, 9.

44 X. Gao, M. P. Zheng, H. J. Lv, Y. Z. Zhang, M. K. Zhu and Y. D. Hou, *Compos. Sci. Technol.*, 2022, **229**, 9.

45 L. C. Wan, W. R. Tian, N. J. Li, D. Y. Chen, Q. F. Xu, H. Li, J. H. He and J. M. Lu, *Nano Energy*, 2022, **94**, 9.

46 M. Q. Wu, Z. Y. Zhang, Z. R. Liu, J. M. Zhang, Y. L. Zhang, Y. M. Ding, T. Huang, D. L. Xiang, Z. Wang, Y. J. Dai, X. Y. Wan, S. B. Wang, H. L. Qian, Q. J. Sun and L. L. Li, *Nano Today*, 2021, **37**, 12.

47 N. Jia, Q. Xing, X. Liu, J. Sun, G. M. Xia, W. Huang and R. Song, *J. Colloid Interface Sci.*, 2015, **453**, 169–176.

48 T. D. Raju, S. Veeralingam and S. Badhulika, *ACS Appl. Nano Mater.*, 2020, **3**, 4777–4787.

49 K. M. Peng, T. Zou, W. Ding, R. N. Wang, J. S. Guo, J. J. Round, W. P. Tu, C. Liu and J. Q. Hu, *RSC Adv.*, 2017, **7**, 24903–24913.

50 A. Ali, L. B. Chen, M. S. Nasir, C. Wu, B. L. Guo and Y. D. Yang, *Environ. Chem. Lett.*, 2022, 18, DOI: **10.1007/s10311-022-01537-3**.